Advanced Materials Interfaces

ADVANCED MATERIALS INTERFACES Open Access

www.advmatinterfaces.de

RESEARCH ARTICLE OPEN ACCESS

Thermal Enhancement of TADF-OLED Performance: Size of Active Area Matters

Demyd V. Pekur[1] | Denis M. Khmil[1] | Petro S. Smertenko[1] | Alexander N. Fedoryak[1] | Chih-Hung Ko[2] | Chih-Hao Chang[2] | Dovydas Blazevicius[3] | Gintare Krucaite[3] | Saulius Grigalevicius[3] | Oleg P. Dimitriev[1]

[1]V. Lashkaryov Institute of Semiconductor Physics NAS of Ukraine, Kyiv, Ukraine | [2]Department of Electrical Engineering, Yuan Ze University, Taoyuan, Taiwan | [3]Department of Polymer Chemistry and Technology, Kaunas University of Technology, Kaunas, Lithuania

Correspondence: Oleg P. Dimitriev (dimitr@isp.kiev.ua)

Received: 1 June 2026 | **Revised:** 10 August 2026 | **Accepted:** 19 August 2026

Keywords: active size area | energy upconversion | OLED | thermal management | thermally activated delayed fluorescence

ABSTRACT

Temperature significantly impacts the performance of light-emitting diodes, typically causing degradation as they heat up. However, OLEDs using thermally activated delayed fluorescence (TADF) emitters show a remarkable increase in electroluminescence up to one order of magnitude, depending on the applied voltage, as temperature climbs from 18 to 50°C. This work reveals that this heat-induced boost in TADF-OLED performance is also influenced by the device's active area. By varying the active area from 225 to 4 mm^2, we show that the thermal enhancement in both electroluminescence and external quantum efficiency (EQE) noticeably declines in smaller devices, with the smallest device showing performance deterioration at high temperatures. While large-area devices demonstrate up to a tenfold increase in EQE near the turn-on voltage due to heating, their EQE remains low compared to smaller devices, with heat only partially bridging this gap. The size-dependent behaviour is linked to factors like interface non-uniformity and aging in large areas, making these devices prone to burnouts that further worsen with thermal runaway. Since OLED performance often decreases with larger sizes, the ability of heating to mitigate this effect supports the effective use of large displays at higher temperatures and suggests TADF-OLEDs can convert waste heat into light efficiently.

1 | Introduction

Size-dependent performance of light-emitting diodes (LEDs) presents significant challenges for both manufacturing and practical applications. This dependence is observed in inorganic LEDs as well as organic light-emitting diodes (OLEDs), particularly at the micrometer scale, though the mechanisms and consequences differ substantially [1]. For inorganic LEDs (GaN-based), scaling down to the micron level (Micro-LEDs, <10 µm) introduces serious technical hurdles, most notably efficiency loss [2, 3]. As the crystal area decreases and the perimeter-to-area ratio increases, non-radiative Shockley–Read–Hall (SRH) recombination at etched sidewalls intensifies, exacerbating current crowding and reducing external quantum efficiency (EQE) [4, 5]. Smaller diodes reach peak efficiency at higher current densities than larger chips [6], and it has been reported that smaller GaN-based micro-LEDs exhibit lower maximum efficiency [7, 8]. On the positive side, the higher surface-to-volume ratio of smaller micro-LEDs improves heat dissipation, enabling operation at extremely high current densities without overheating compared to mini-LEDs or conventional LEDs [9]. Small LEDs also tend to exhibit more stable emission wavelengths, reducing red-shift due to self-heating [3]. Interestingly, EQE in multiple-quantum-well InGaN/AlGaN near-ultraviolet micro-LEDs can improve in smaller devices, since larger ones suffer from pronounced current crowding that drives carrier overflow from the active region, lowering EQE at high current densities [10].

For OLEDs, size effects manifest differently, primarily influencing durability and stability [1]. Unlike inorganic LEDs, large-area OLEDs face voltage drops and current-crowding issues. Nevertheless, larger pixel sizes are generally preferred for long-term reliability, as they achieve the required brightness at lower current densities, which is critical for extending the lifetime of organic materials. Sidewall effects on quantum efficiency are negligible in OLEDs, but large-area devices often suffer from short-circuiting, luminance non-uniformity, hot spots, efficiency reduction, and heat generation. At small sizes, OLEDs remain inferior to Micro-LEDs in peak brightness and burn-in resistance [11].

Despite extensive research on micro-LEDs, systematic studies of size effects at the macroscale (mm–cm range) remain rare and not systematic. Recently, we observed significant enhancements in electroluminescence and EQE of OLEDs based on thermally activated delayed fluorescence (TADF) emitters when the temperature increased from 18°C to 50°C [12]. Near the turn-on voltage, this enhancement reached factors of 5–7. However, since EQE values at this bias are inherently small, the thermally induced boost did not yield record efficiencies, which remain far below the theoretical maximum of ~40% [13]. Given that smaller OLEDs typically perform better, this work investigates whether devices of identical composition but reduced size could exhibit similar thermally induced effects, potentially approaching record EQE values. Instead, we found a more complex size-dependent behavior, where variations in current dynamics—particularly the interplay of drift and diffusion components—govern the main performance trends.

2 | Results

2.1 | Device Fabrication

To examine the electroluminescent (EL) performance of TADF OLEDs, two devices incorporating yellow- and green-emitting TADF materials were fabricated and are referred to as the Y and G devices, respectively. The commercially available yellow emitter NAI-DMAC, *N*-(4-tert-butylphenyl)-1,8-naphthalimide-9,9-dimethyl-9,10-dihydroacridine [14], was used, while the green emitter EM2, (4-(9*H*-carbazol-9-yl)phenyl)(4-(3-(diphenylamino)-9*H*-carbazol-9-yl)phenyl)methanone, was synthesized in our earlier work [15]. An effective host material must ensure balanced charge transport, enable exothermic energy transfer to guest molecules, and provide strong exciton confinement. Since exciplexes form between hole- and electron-transport materials, exciplex-based hosts typically offer improved charge transport and reduced operating voltages. Based on previous results, an exciplex host composed of the donor TCTA (4,4′,4″-tris(carbazol-9-yl)triphenylamine) and the acceptor CN-T2T ((1,3,5-triazine-2,4,6-triyl)tris(([1,10-biphenyl]-3-carbonitrile))) was selected for both devices, as it satisfies these requirements [16].

In both OLEDs, CN-T2T was also employed as the electron transport layer (ETL) to ensure compatibility with the host system. To achieve efficient hole injection and proper alignment of the highest occupied molecular orbital (HOMO) levels, a double hole transport layer (HTL) structure was implemented using TAPC (1,1-bis[(di-4-tolylamino)phenyl]cyclohexane) and TCTA. This arrangement provides stepwise hole transport, facilitating smooth hole injection into the emitting layer (EML) [17]. Using common materials across the HTL (or ETL) and EML further minimizes interfacial energy barriers, suppresses charge accumulation, and enhances current density and overall device performance. TAPC was also used as a host for MoO_3 to form a p-type hole-injection layer (HIL), thereby promoting efficient hole injection via band bending at the anode interface.

Accordingly, the optimized structures of the yellow (Y) and green (G) OLEDs were as follows: ITO (120 nm)/TAPC doped with 20 wt.% MoO_3 (10 nm)/TAPC (35 nm)/TCTA (5 nm)/TCTA:CN-T2T (1:1) doped with 1 wt.% NAI-DMAC or 5 wt.% EM2 (20 nm)/CN-T2T (50 nm)/LiF (1.2 nm)/Al (120 nm), where LiF and Al served as the electron injection layer and cathode, respectively. The molecular structures of the materials and schematic device architectures are shown in Figure 1a,b.

2.2 | Basic Characteristics of the OLEDs at Room Temperature

We found that device characteristics and performance exhibit distinct differences depending on active area size, even at room temperature. First, changes in active area size affect the EL spectra, which also depend on the emitter used. For the Y device, EL spectra closely match the PL emission spectra of the dye films, showing a maximum at ~590 nm, independent of device size and applied bias, except for a small bump at ~460 nm observed at high voltage—consistent with the PL spectra of the diluted dye solution. In contrast, the G device shows more complex behavior. A small-area G device at low bias (near the turn-on voltage) produces an EL spectrum resembling the PL spectrum of a thin film, with a maximum near 540 nm. At high bias (6 V), the large-area G device exhibits EL similar to the PL spectrum of the diluted dye solution, with a maximum at 492 nm. Intermediate conditions yield spectra between these two cases (Figure 2a,b). These differences suggest that emitter aggregation tendencies vary with device area. In the Y device, NAI-DMAC molecules predominantly exist in the aggregated state, whereas in the G device, large-area structures and high biases favor the monomeric form of EM2, while smaller areas and low biases promote aggregation. Although both emitters are doped into the TCTA:CN-T2T matrix at concentrations of 1 and 5 wt% (Figure 1b), their distinct diffusion and crystallization behaviors are influenced by device size and applied bias.

Second, device area size significantly impacts current behavior. Large-area devices exhibit higher current density at low biases (near and below the turn-on voltage), indicating the presence of defects or burnout spots that allow current shortcuts. Conversely, small-area devices show lower current density at low bias but higher density at high biases (>4 V), resulting in a steeper overall current–voltage dependence (Figure 2c,d). Notably, J–V curves of small-area devices display more pronounced diode-like behavior, with current density spanning up to seven orders of magnitude and clear turn-on voltages at 2.6 V (Y device) and 2.2 V (G device). Large-area devices, however, span only three orders of magnitude, with shifted turn-on voltages at 3.0 and 2.8 V,

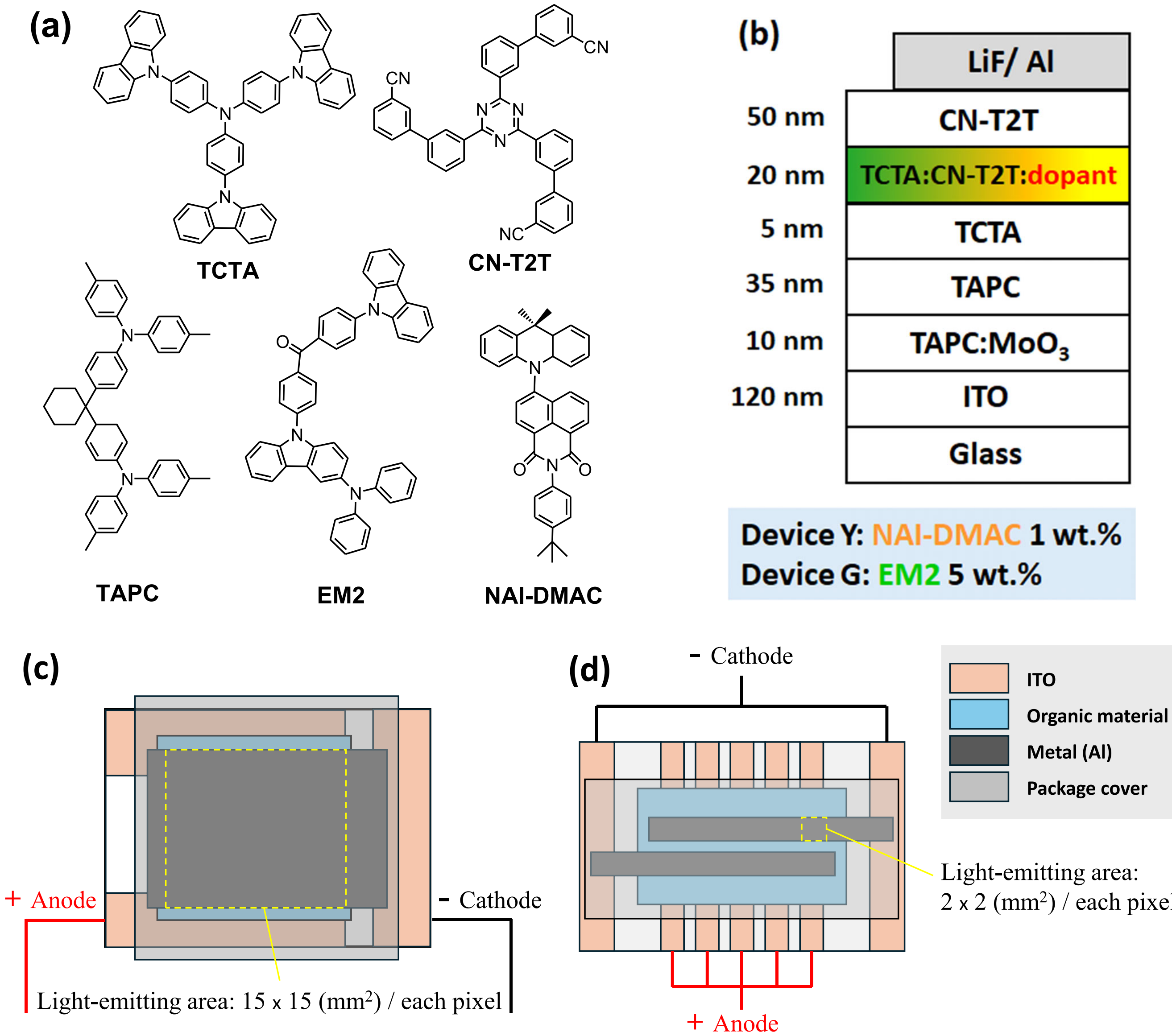

FIGURE 1 | (a) Structural drawings of the materials used; (b) schematic structures of the fabricated TADF OLEDs; device architecture design of (c) large-area and (d) small-area.

respectively. The smeared current–voltage characteristics suggest blurred interfaces in large-area OLEDs, which is reasonable given the difficulty of fabricating sharp interfaces over large areas.

Finally, performance worsens as device size increases (Table 1). Both EQE and power efficiency are higher in small-area devices and increase as current density decreases (Figure 2e,f). In contrast, larger devices show suppressed EQE and power efficiency beginning at low current densities, though values converge at high current densities (>10 mA/cm^2).

As an example, we checked the changes in EQE and power efficiency for the G device as a function of the device active area, varying the latter from 0.04 to 2.25 cm^2 by the different number of OLED pixels involved. It was observed that there was a gradual drop in both EQE and power efficiency as the active area increased, with high variation of their values at small current densities, while all the curves merged at high current densities (Figure 3). The different behavior of EQE and power efficiency versus current density becomes clear when taking into account the above result (Figure 2d) indicating that the turn-on voltage corresponds to current density of ~3×10^{-5} and ~4×10^{-1} mA/cm^2 for the small-area and large-area devices, respectively, which means that the corresponding curves are limited from the lower values of the current densities (Figure 3, note that we could not measure EL at current densities smaller than 10^{-2} mA/cm^2 due to instrument limitations). But the maximum value of EQE and power efficiency is shifted to the higher current densities too, observed at about 0.1, 1, and 10 mA/cm^2 for the active device areas of 0.08, 0.2, and 2.25 cm^2, corresponding to EQE of 9.6, 5.0, and 3.0% and power efficiency of 31.3, 13.3, and 5.3 lm/W, respectively (Figure 3).

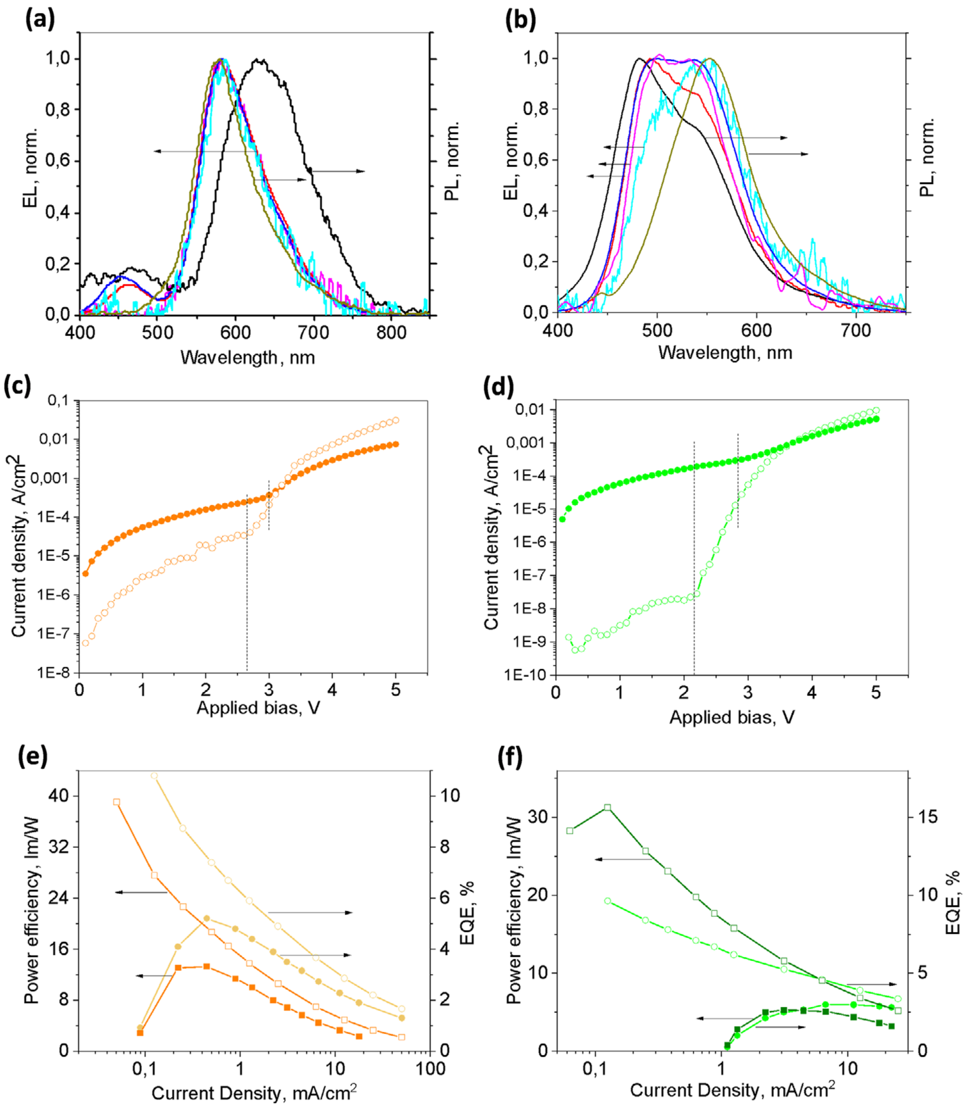

FIGURE 2 | (a,b) Normalized EL spectra of small-area device at applied biases of 2.9 V (light-blue) and 6 V (blue) and large-area device at applied biases of 2.9 V (magenta) and 6 V (red), compared to PL spectra of solution (black) and film (dark-yellow); (c,d) current-voltage characteristics of small-area devices (open symbols) and large-area devices (solid symbols); (e,f) power efficiency and EQE of small-area devices (open symbols) and large-area devices (solid symbols), based on (a,c,e) NAI-DMAC and (b,d,f) EM2 emitters.

TABLE 1 | EL characteristics of the tested devices of different sizes (0.04 cm^2 vs. 2.25 cm^2).

Device	Emitter	η_{ext} (%)[a]	η_P (lm/W)[a]	V_{on} (V)	λ_{max} (nm)	CIE1931 coordinates (x, y)
Y	NAI-DMAC	10.8/5.2	39.1/13.3	2.6/3.0	584/582	(0.53, 0.46)/ (0.53, 0.45)
G	EM2	18.2/3.0	31.3/5.3	2.2/2.8	539/495	(0.33, 0.52)/ (0.40, 0.53)

[a]Maximum efficiency; [η_{ext}: external quantum efficiency; η_P: power efficiency].

2.3 | Effect of Temperature

We found that heating OLED devices to moderate temperatures, up to 50°C, induces changes in both EL (Figures S1–S4) and current behavior. Importantly, these changes are fully reversible upon cooling back to room temperature, as demonstrated in our previous study (see Ref. [12] and Figure S5). The temperature dependence of currents in large-area OLEDs was analyzed earlier [12], and similar behavior is confirmed here (Figure 4). Specifically, OLEDs with an active area of 2.25 cm^2 exhibit two distinct regimes: an abnormal region, where currents remain nearly unchanged or even decrease with temperature, and a normal region, where currents increase with temperature. These regimes occur at low and high applied biases, respectively, with the

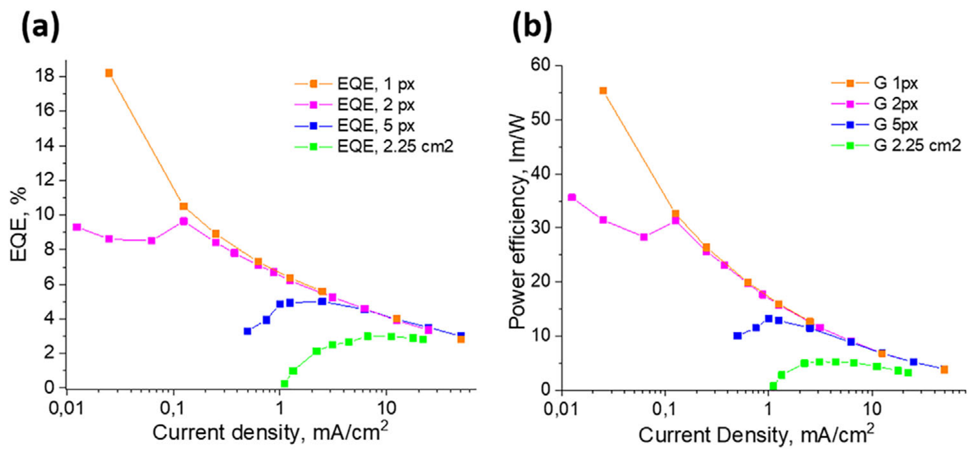

FIGURE 3 | (a) External quantum efficiency and (b) power efficiency versus current density of the G device as a function of the active device area: 0.04 cm^2 (orange), 0.08 cm^2 (pink), 0.2 cm^2 (blue), and 2.25 cm^2 (green).

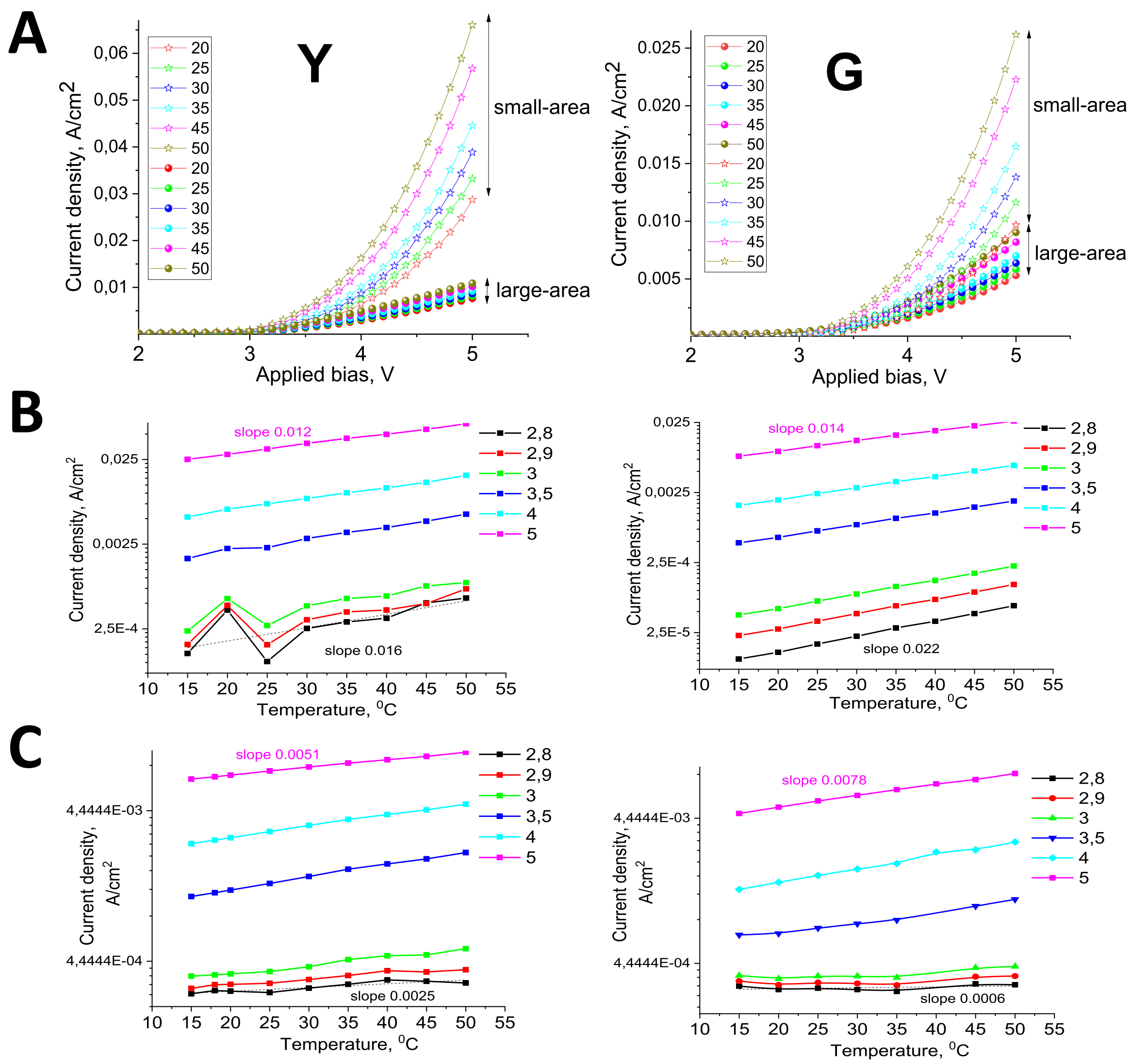

FIGURE 4 | Current density as a function of (a) applied bias and (b,c) temperature of (b) small-area (0.04 cm^2) and (c) large-area (2.25 cm^2) Y and G devices. In (a), J-V curves for both small-area (stars) and large-area (spheres) devices are shown; the temperature for each curve is indicated in the legend. In (b,c), dashed lines are the linear fit of current-temperature curves and the applied bias for each curve is indicated in the legend.

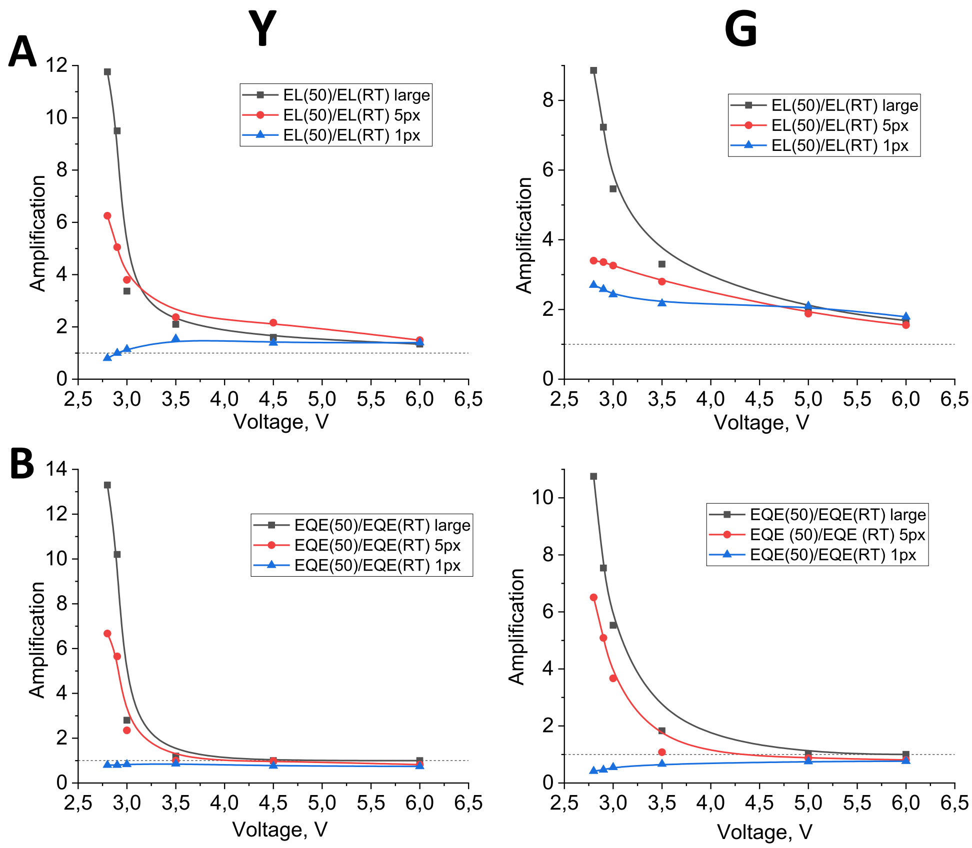

FIGURE 5 | Amplification of (a) EL and (b) EQE of the Y and G devices of the different active areas: 0.04 cm^2 (blue), 0.2 cm^2 (red), and 2.25 cm^2 (black); the curves are the guide for the eye.

current–temperature slope close to zero at 2.8 V and increasing at higher biases (Figure 4b,c). The abnormal region is more pronounced in the G device, while in the Y device it is confined to a narrower temperature interval (~15–25°C).

By contrast, small-area devices display only the normal regime, with currents consistently increasing with temperature regardless of applied bias (Figure 4b). This behavior is typical of disordered semiconductors, where charge transport occurs via thermally activated hopping [18, 19]. Moreover, small-area devices show a steeper current–temperature dependence compared to the normal regime of large-area devices, with slopes approximately twice as high at 5 V bias.

Electroluminescence also increases with temperature, depending on the applied bias, as reported previously [12]. The mechanism of such enhancement is due to increasing rates of RISC (k_{RISC}) with temperature,

$$k_{RISC} \sim \exp\left(-\frac{\Delta E_{ST}}{kT}\right) \quad (1)$$

where ΔE_{ST} is the S_1 to T_1 energy difference. Taking ΔE_{ST} = 50 meV for NAI-DMAC [20], Equation (1) yields boosting k_{RISC} by a factor of 1.4 upon the temperature increase from 20 to 50°C, which agrees well with the EL enhancement at 6 V for the Y devices (Figure 5a).

However, the magnitude of enhancement—calculated as the ratio of EL intensity at 50°C to that at room temperature (Figures S1–S4)—varies with device size. Large-area OLEDs exhibit substantial EL enhancement, up to an order of magnitude, near the turn-on voltage (Figure 5a). In smaller devices, this enhancement diminishes, with virtually no gain observed near the turn-on voltage for the small-area Y device (0.04 cm^2). At higher biases, EL enhancement decreases across all devices, falling below a factor of two near 6 V.

Significant amplification of EL with temperature, combined with only modest current changes near the turn-on voltage, results in a pronounced enhancement of EQE at elevated temperatures for large-area devices. At 50°C, EQE increases by nearly an order of magnitude—specifically, by a factor of 13 for the Y device and 11 for the G device (Figure 5b). However, this enhancement rapidly diminishes with increasing bias, with no net gain observed near 5 V.

For medium-sized devices (active area 0.2 cm^2), the thermally induced EQE gain is smaller, reaching a factor of 6 near the turn-on voltage but dropping below unity at higher voltages (>4.5 V). In the smallest device (0.04 cm^2), no EQE enhancement was observed; in fact, the ratio of EQE at 50°C to that at room temperature remains below unity across the entire bias range (Figure 5b). Thus, heating improves performance only in relatively large-area OLEDs, while their absolute EQE values remain lower than those of small-area devices (see Figure 3).

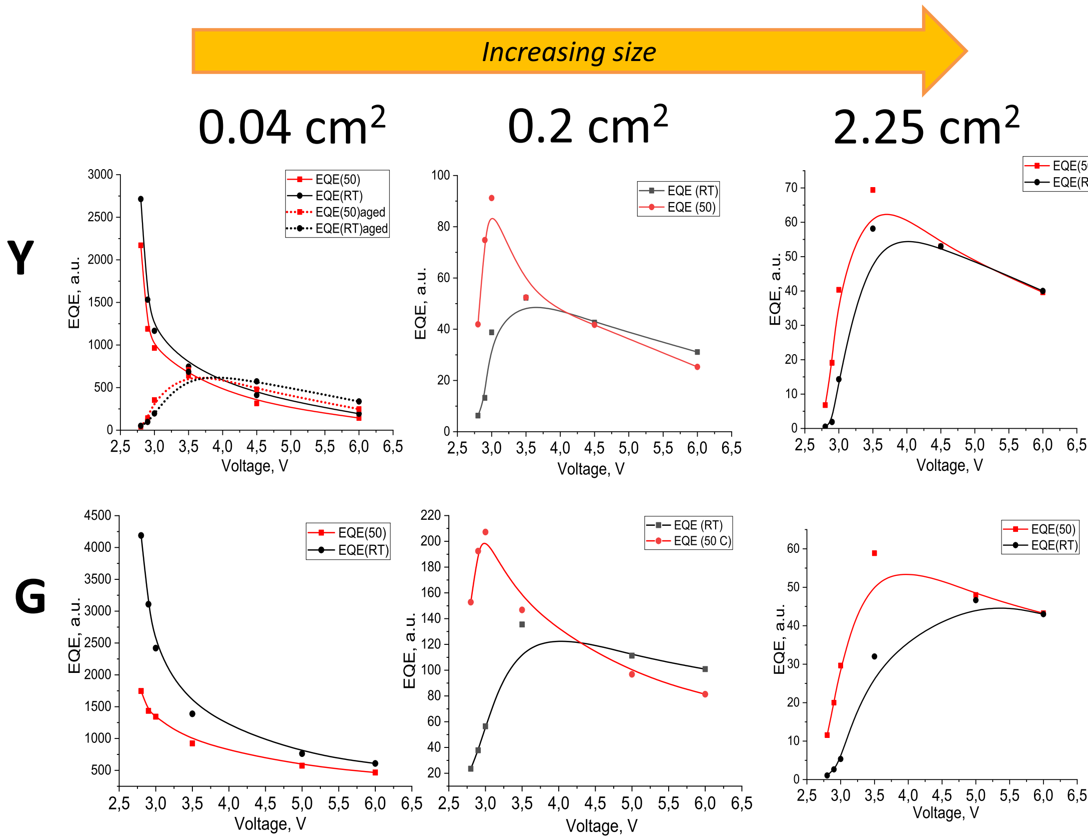

FIGURE 6 | Relative EQE as a function of the applied bias of the Y and G devices of the different active areas is indicated. The curves are guides for the eye: black curves correspond to room temperature, and red ones to 50°C. Dotted curves correspond to the 4-week-aged small-area Y device.

Bias-dependent EQE trends at 50°C and room temperature are shown in Figure 6. Elevated temperature consistently degrades the performance of small-area devices across all biases. In contrast, medium-sized OLEDs (0.2 cm^2) exhibit improved EQE in a limited bias range (<4 V), while large-area devices show enhancement across the entire bias range, though their EQE values remain significantly lower than those of small-area OLEDs. Aging also affects EQE: after four weeks of storage in a dry atmosphere with no operation, the small-area Y device displayed modified behavior, resembling that of the medium-sized device, with EQE gain restricted to biases below 4 V (Figure 6, dotted curves).

Since OLED performance generally worsens with increasing active area, heating can be regarded as a compensating factor, partially offsetting this decline and enabling the operation of large-area devices at elevated temperatures. This finding highlights the potential of TADF-based OLEDs for thermal energy upconversion, where waste heat is harnessed to boost light emission. The efficiency of converting supplied thermal energy into optical output can be roughly estimated by considering the heat flux from the oven: assuming the oven's electrical power is fully converted into heat (W_{heat}), part of which is absorbed by the device (W_{in}, see Figures S6 and S7 and description in Supporting Information), and comparing the excess optical power at high temperature to the optical power at room temperature, $W_{opt}(RT)$:

$$\eta = \left(\left(kW_{\text{opt}} \left(RT \right) - 1 \right) / W_{\text{in}} \right) \times 100\% \tag{2}$$

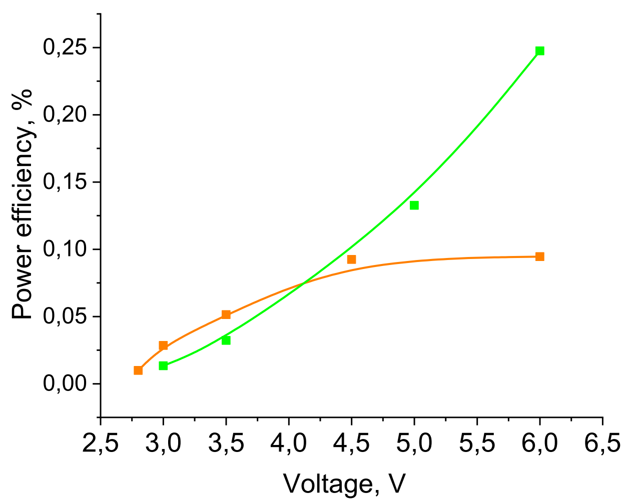

FIGURE 7 | Estimated power efficiency of conversion of thermal energy into energy of light emission as a function of applied bias for the Y (yellow symbols) and G (green symbols) large-area devices.

where η is the power efficiency of the energy conversion, k is the amplification factor of EL at 50°C, and $kW_{opt}(TR)$-1 is the excess of the optical power at 50°C.

The calculated power efficiency for the large-area devices shows increasing values with increasing applied bias (Figure 7). Although thermally induced EL amplification decreases at higher voltage by about one order of magnitude (Figure 5a), the optical power of emission increases by about two orders of magnitude, i.e., from tens of microwatts to milliwatts for biases of 3 and 6 V, respectively. Therefore, even a small thermally induced gain in EL at high voltage results in higher power efficiency compared to η at small voltage. Although the absolute values of power efficiency are small, less than 1%, abundance of the waste heat can compensate for this drawback.

3 | Discussion

The difference in device performance as a function of active area size can be considered from two perspectives. On one hand, a large-area device may be viewed as an equivalent circuit composed of multiple small diodes connected in parallel. In our design, this configuration is realized through an array of pixels (Figure 1d), which collectively reproduce the behavior of a large-area device (Figure 1c), while each individual diode can exhibit distinct operating characteristics (see, for example, Figure 3).

On the other hand, performance deterioration can be attributed to the quality of interfacial layers. Larger interfaces tend to exhibit greater variation in energy barriers, charge accumulation, and current density depending on the interface spot, all of which influence overall device operation. Moreover, large interfaces are often associated with uneven current distribution, arising from inhomogeneous contact resistivity between the ITO and Al electrodes, which varies with distance from the metal contact [21].

Deterioration of device performance is primarily driven by defects and burnout that emerge during operation. In principle, the initial defect density should be independent of device size if the structures are fabricated identically, meaning larger areas simply contain proportionally more defects. This becomes critical because, although degradation of individual diodes occurs randomly in the equivalent parallel-diode scheme, the burnout of a single diode can short-circuit the entire array. As a result, large-area devices exhibit higher current densities at low applied biases and lose the characteristic diode-like behavior in their *J*–*V* curves (Figure 2c,d).

The burnout mechanism can be explained by thermal runaway: slight variations in forward voltage among parallel-connected diodes cause one diode to carry a disproportionate share of the current. The diode with the lower forward voltage heats up, its voltage drops further, and it draws even more current until failure occurs. Thus, while diodes nominally share the total current, imperfect matching leads to inefficient and unstable operation.

This breakdown in uniform operation among neighboring diodes in the parallel array results in inhomogeneous heating across the OLED surface, as confirmed by IR imaging (Figure 8). This observation aligns with recent studies showing that nanoscale hotspots in multilayer OLEDs—sometimes only tens of nanometers wide—can carry currents 10–100 times higher than surrounding regions, greatly accelerating local degradation and reducing overall device lifetime [22]. We observed that even in devices producing apparently uniform EL emission across the surface, IR imaging reveals localized hotspots indicative of potential leakage (Figure 8a). As OLEDs deteriorate, the temperature distribution becomes increasingly inhomogeneous (Figure 8b). Interestingly, in severely degraded OLEDs that emit light only from small regions of the active area, the hottest spots do not coincide with the emission sites. Instead, dark leakage regions primarily determine the surface temperature (Figure 8c). Burnout regions can then expand, as their local temperature is higher than that of neighboring areas. Because the probability of a single burnout increases with device area, its subsequent expansion has a stronger impact on large-area structures. Statistically, larger burnout regions are therefore observed in large-area OLEDs (Figure 9).

A second factor influencing performance is the quality of interfacial layers. In large-area devices, achieving high-quality interfaces is more challenging due to the mismatch between evaporation source size and substrate dimensions, leading to non-uniform thickness, angle-dependent deposition, and occasional layer intermixing. The resulting smeared interfaces degrade diode-like behavior, as evidenced by suppressed current densities at high applied biases and smoother J–V curves in large-area OLEDs (Figure 2c,d). This change in current behavior can be attributed to increasing disorder associated with a higher concentration of structural traps. These traps enhance carrier scattering, even under weak electric fields, and compete with carrier trapping by the triplet states of TADF molecules, thereby reducing electroluminescence. Moreover, smeared interfaces likely facilitate diffusion processes that extend structural defects. Once formed, such defects lower interfacial energy barriers and expand over time due to enhanced diffusion. Although defect densities appear similar across devices, larger defect sizes are consistently observed in large-area OLEDs (Figure 9).

As shown, heating somewhat compensates for the deterioration effects in the large-area devices, improving their performance. This phenomenon cannot be attributed to annealing effects or interface recovery, as device performance is reversible upon cooling [12]. A better understanding of the above compensation effect can be obtained by calculating the dimensionless sensitivity, *DS*, based on current-voltage characteristics of the OLEDs:

$$DS\,(V) = \frac{d\log\,(J)}{d\log\,(V)} = \frac{dJ}{dV}\frac{V}{J} \tag{3}$$

The *DS* behavior reflects carrier injection and recombination processes in OLEDs. Monomolecular recombination ($DS = 2$) typically corresponds to nonradiative loss mechanisms, where defects trap a single electron or hole and recombine without light emission (the Shockley–Read–Hall mechanism). This process dominates low current densities and reduces injection efficiency. In contrast, efficient OLED operation relies on bimolecular recombination ($DS = 1.5$)—a second-order process in which an electron and a hole directly recombine to produce light.

Bimolecular recombination is observed in both small- and large-area OLEDs at applied biases between ~1 and 2.5 V, i.e., below the turn-on voltage, where all injected carriers are captured by the emitter (Figure 10). At higher voltages, where OLED emission occurs, *DS* rises sharply. The key distinction between small- and large-area OLEDs lies in the *DS* peak value and its

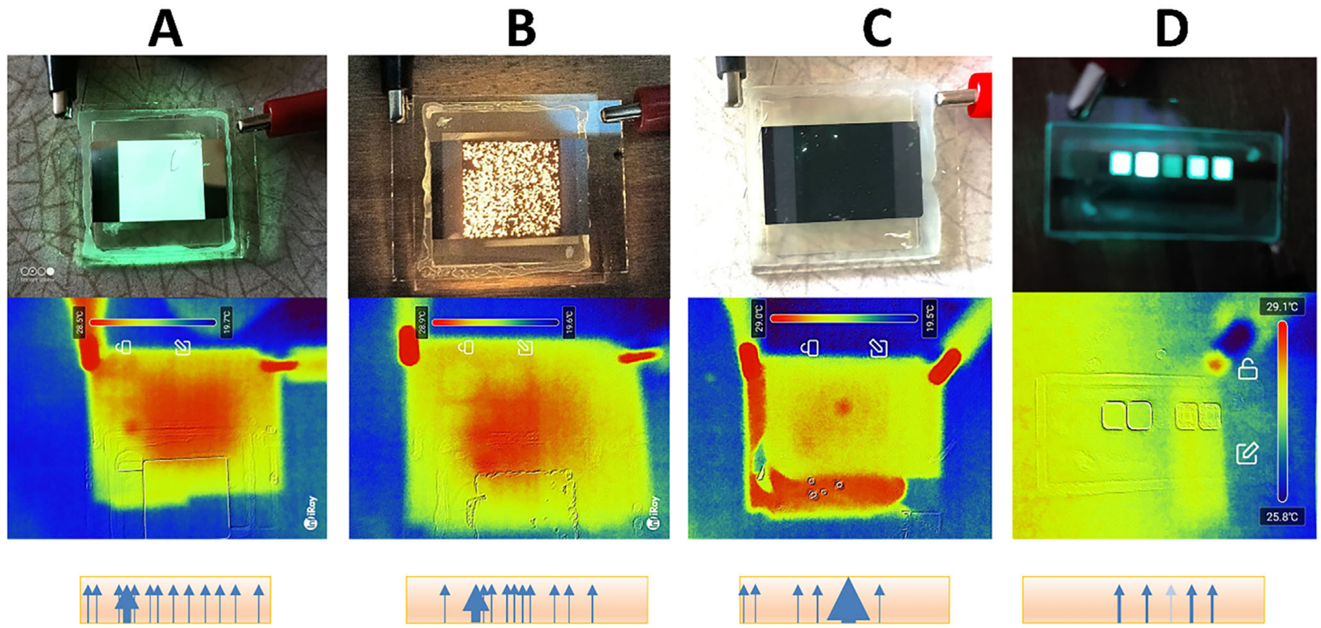

FIGURE 8 | Top: Photographs of (A–C) large-area and (D) small-area OLEDs under operation at 6 V; Middle: IR images of the same OLEDs; Bottom: Schematics of the current flow distribution across the OLED, with thick arrows indicating shortcuts. (A) Virtually perfect OLED with no degradation; (B) OLED with modest degradation; (C) OLED with high degradation; (D) a set of small-area OLEDs connected in parallel, showing a different extent of degradation.

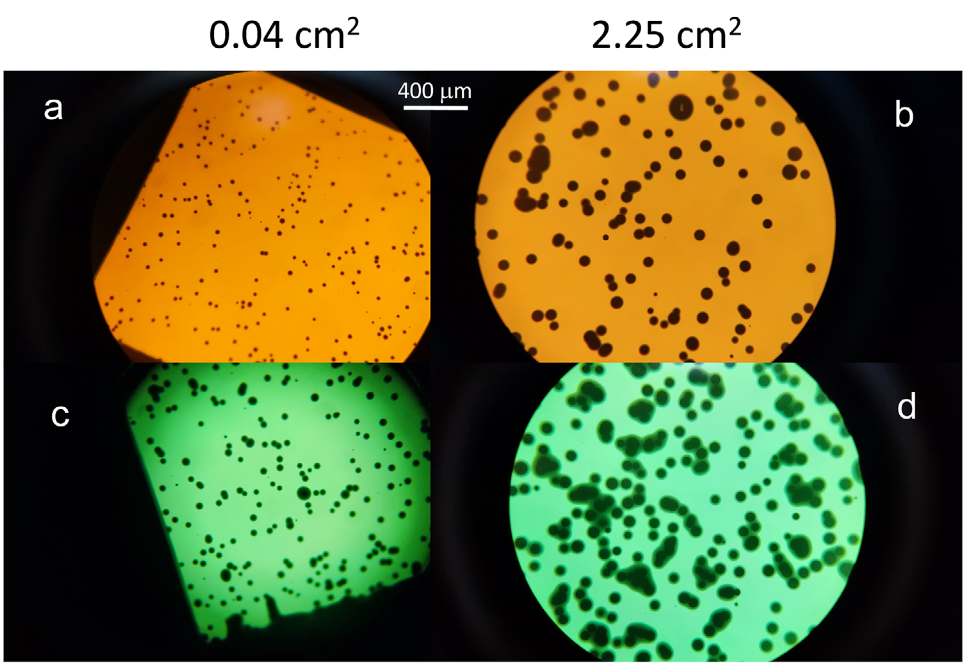

FIGURE 9 | Micrographs of (a,c) small-area and (b,d) large-area Y and G devices under applied bias of 6 V.

temperature dependence. In small-area OLEDs, the *DS* peak is about twice that of large-area devices and remains nearly temperature-independent. Conversely, in large-area OLEDs, the *DS* maximum increases and shifts to lower voltages with rising temperature, approaching the *DS* behavior of small-area devices.

This behavior can be explained by the competition between diffusion and drift currents under varying voltages and temperatures. Diffusion current is highly sensitive to temperature, as described by the Einstein relation between diffusivity D and mobility μ:

$$D = \mu kT/q \tag{4}$$

Drift current, while enhanced at higher temperatures in disordered semiconductors due to improved carrier activation, is simultaneously hindered by increased scattering, which

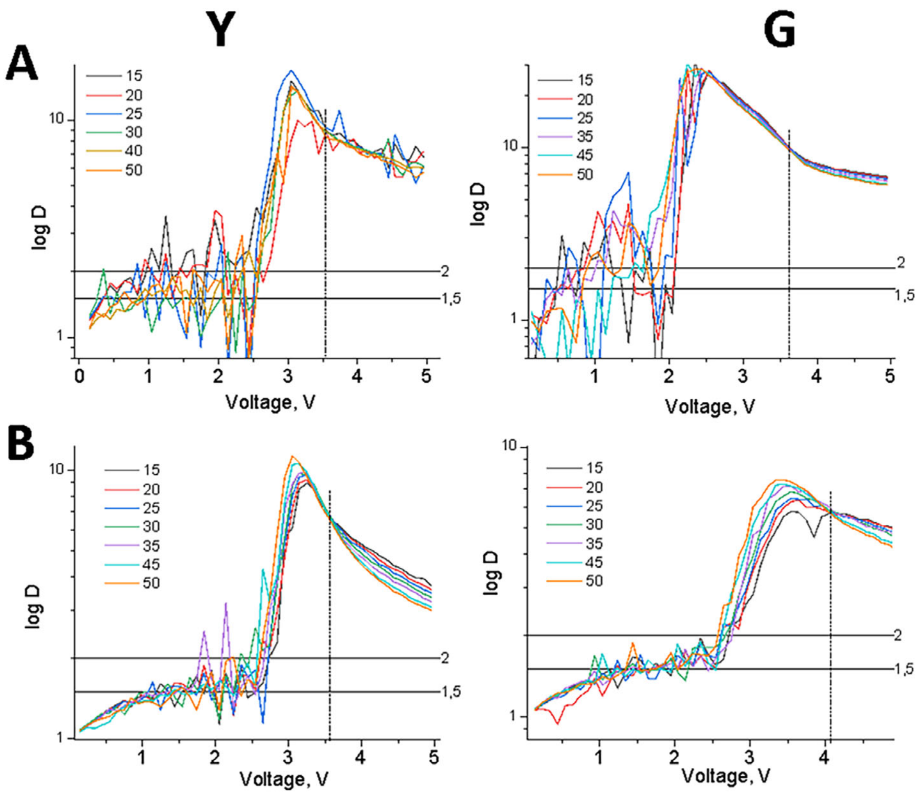

FIGURE 10 | Logarithm *DS* of (a) small-area (0.04 cm^2) and (b) large-area devices (2.25 cm^2) as a function of applied bias and temperature (indicated in legend in Celsius). The vertical dashed lines mark the isosensitive points.

suppresses the drift component. In large-area OLEDs, drift current is less effective than in small-area devices because of scattering from defects and shortcuts caused by burnouts. At elevated temperatures and low biases, diffusion current becomes dominant, compensating for drift-current losses by redistributing carriers from regions of high concentration to regions of low concentration (see Figure 8, bottom line). This inference is supported by the smoother increase in current density observed in large-area OLEDs compared to small-area devices. Such behavior resembles a healing effect, where burnout regions exert less influence on current flow at high temperatures, thereby stabilizing device operation.

4 | Experimental

4.1 | Materials

Synthesis of EM2 emitter is described in Ref. [15]. All other organic materials were obtained from Shine Materials Technology and purified by temperature-gradient sublimation under high vacuum before use. ITO-coated glass substrates were cleaned by ultrasonication in deionized water and organic solvents, followed by a 5 min UV plasma treatment. Organic and metal layers were deposited by thermal evaporation in a vacuum chamber with a base pressure below 10^{-6} Torr, with the entire fabrication process carried out without breaking vacuum. The deposition rate for organic layers was maintained at approximately 0.1 nm/s. The shadow mask defines large-area and small-area light-emitting devices with dimensions of 15 × 15 and 2 × 2 mm^2, respectively (see Figure 1c,d).

4.2 | Measurements

UV–vis absorption and photoluminescence (PL) emission spectra were recorded using an AvaSpec-2048 spectrometer coupled to a 600 µm optical fiber. A thermoelectrically cooled CCD detector was used to minimize noise in the detected light. Stock solutions of NAI-DMAC in toluene and EM2 in dichloromethane (DCM) were prepared at a concentration of 10^{-3} M and subsequently diluted to 10^{-5} M for optical measurements. All measurements were carried out in a 10 mm quartz cuvette, with the corresponding pure solvent used as a reference. Excitation was provided by a 254 nm diode and diode-pumped solid-state lasers operating at 365 and 405 nm.

Temperature-dependent studies of EL in OLED devices were performed using a custom-built thermostat equipped with an oven, which was heated at a rate of approximately 1°C per minute. Temperature was monitored using a thermocouple positioned between the oven and the rear side of the OLED, with additional correction applied based on a separately determined temperature gradient between the rear and front surfaces of the device. The resulting temperature accuracy was ±1°C. EL spectra as a function of temperature were recorded using the AvaSpec-2048 spectrometer.

The luminous flux and spectral characteristics of radiation were determined using an Everfine HAAS-2000 matrix spectroradiometer integrated with an integrating sphere with a diameter of 0.3 m. The use of an integrating sphere enabled the implementation of the condition of full spatial integration of radiation, regardless of the angular intensity distribution, which is critically important for the correct determination of the total luminous flux and spectral power of radiation. Before the measurements, the system was calibrated using a reference light source traceable to national standards, ensuring reproducible results and a measurement error of no more than ±3%. For each operating point (*J, V*), the spectral distribution of radiation, the integrated luminous flux, and the electric power were recorded, which allowed calculation of the luminous efficiency and other derived parameters.

Electrical parameters, in particular, current-voltage characteristics, power consumption, and stabilized power supply mode, were determined using a precision Keithley 2635B measuring source. The device operated in the Source-Measure Unit mode, which allowed simultaneous setting of the voltage or current and recording the corresponding electrical responses with high resolution. Measurement control was carried out in an automated mode using a software interface, which ensured the formation of a series of measurements and reduced the impact of random errors. Temperature measurements of *J-V* characteristics were performed in stationary thermal mode after the sample temperature stabilized.

IR images of the samples in the 8–14 μm spectral range were collected by an InfiRay camera integrated with a Doogee V20 Pro smartphone.

5 | Conclusion

In this work, we confirmed that heat is a significant factor enhancing the performance of TADF-based OLEDs and we demonstrated that this enhancement also depends on the device's active area. By varying the active area from 4 to 225 mm^2, we showed that heat substantially improves electroluminescence and EQE in large-area devices—by nearly an order of magnitude near the turn-on voltage. However, the enhancement diminishes as the device area decreases, eventually becoming a thermal deterioration factor for EQE in small-area OLEDs.

This size-dependent performance was attributed to several factors. First, large panels require larger substrates, which increase the sheet resistance of the transparent conductive electrode (ITO). This causes a voltage drop across the panel, so pixels farther from the power supply receive less voltage and appear dimmer. Second, large-area interfaces suffer from non-uniformity and uneven aging of pixels, leading to brightness variations across the screen. Third, large interfaces are more vulnerable to defects and burnouts, which expand through thermal runaway: slight variations in forward voltage between spots cause one spot to carry most of the load, raising local temperature, accelerating material degradation, and reducing brightness more rapidly.

Interestingly, specific current behavior arising from the competition between drift and diffusion components—where diffusion dominates at high temperatures—helps compensate for drift-current losses caused by defects and burnout regions in large-area OLEDs. These results highlight the potential of large-area TADF-based OLEDs as thermally assisted light-emitting devices, where moderate waste heat can partially offset efficiency losses associated with increasing area.

The efficiency of thermal energy upconversion into light emission was found to be small but increasing with applied voltage, reaching up to 0.25% for the G device. Although the power efficiency of heat-to-light conversion remains below 1%, the abundance of waste heat can be considered as a useful factor, ultimately improving OLED panel performance.

Author Contributions

D.P., D.K. and P.S.S.: investigation and formal analysis; C.H.K., D.B., G.K., and A.N.F.: resources and data curation; S.G. and C.H.C.: project administration, supervision, and writing – review and editing; O.D.: conceptualization, investigation, writing – original draft, and project administration.

Funding

This work was supported by the Research Council of Lithuania (Grant No. S-LU-24-7), Ministry of Education and Science of Ukraine (project M/54-2024), and the National Science and Technology Council of Taiwan (NSTC 112-2923-E-155-002-MY4, 113-2221-E-155-014-MY3, and 114-2923-E-155-001-MY3).

Conflicts of Interest

The authors declare no conflicts of interest.

Data Availability Statement

The data that support the findings of this study are available from the corresponding author upon reasonable request.

References

1. Y. Huang, E.-L. Hsiang, M.-Y. Deng, and S.-T. Wu, "Mini-LED, Micro-LED and OLED Displays: Present Status And Future Perspectives," *Light: Science & Applications* 9 (2020): 105, https://doi.org/10.1038/s41377-020-0341-9.

2. J. M. Smith, R. Ley, M. S. Wong, et al., "Comparison of Size-Dependent Characteristics of Blue and Green InGaN microLEDs Down to 1 μm in Diameter," *Applied Physics Letters* 116, no. 7 (2020): 071102, https://doi.org/10.1063/1.5144819.

3. Z. Gong, S. Jin, Y. Chen, et al., "Size-Dependent Light Output, Spectral Shift, and Self-Heating of 400 nm InGaN Light-Emitting Diodes," *Journal of Applied Physics* 107, no. 1 (2010): 013103, https://doi.org/10.1063/1.3276156.

4. J. Nie, Z. Zhang, K. Chen, et al., "Systematic Study On Size And Temporal Dependence Of Micro-LED Arrays For Display Applications," *Photonics Research* 11, no. 4 (2023): 549–557, https://doi.org/10.1364/PRJ.479593.

5. K. Fan, K. Zheng, J. Lv, et al., "Analysis of Size-Dependent Optoelectronic Properties of Red AlGaInP Micro-LEDs," *Optics Express* 31, no. 22 (2023): 36293–36303, https://doi.org/10.1364/OE.503024.

6. W. Tian and J. Li, "Size-Dependent Optical-Electrical Characteristics of Blue GaN/InGaN Micro-Light-Emitting Diodes," *Applied Optics* 59, no. 29 (2020): 9225–9232, https://doi.org/10.1364/AO.405572.

7. F. Olivier, S. Tirano, L. Dupré, B. Aventurier, C. Largeron, and F. &Templier, "Influence of Size-Reduction On The Performances of GaN-Based Micro-LEDs for Display Application," *Journal of luminescence* 191 (2017): 112–116, https://doi.org/10.1016/j.jlumin.2016.09.052.

8. Y. Dai, Z. Wang, S. Dou, et al., "Size-Dependent Characteristics of GaN-Based Micro-LEDs for Simultaneous Display and Wireless Optical Communication," *Chinese Optics Letters* 23, no. 8 (2025): 082501, https://doi.org/10.3788/COL202523.082501.

9. C. Ge, J. Li, G. Wang, K. Su, and X. &Lu, "Size Effect On Optical Performance Of Blue Light-Emitting Diodes," *Journal of Semiconductors* 40, no. 10 (2019): 102301, https://doi.org/10.1088/1674-4926/40/10/102301.

10. A. B. M. H. Islam, T. K. Kim, Y. J. Cha, et al., "Enhanced Size-Dependent Efficiency of InGaN/AlGaN Near-Ultraviolet Micro-LEDs," *Applied Physics Letters* 126, no. 4 (2025): 043503, https://doi.org/10.1063/5.0237557.

11. J. W. Park, D. C. Shin, and S. H. Park, "Large-Area OLED Lightings And Their Applications," *Semiconductor Science and Technology* 26, no. 3 (2011): 034002, https://doi.org/10.1088/0268-1242/26/3/034002.

12. D. Kuznetsova, S. W. Huang, F. C. Fan, et al., "Heat Upconversion Into Visible Light By Thermal Management of OLEDs Based on TADF Materials," *Communications Materials* 7 (2026): 183, https://doi.org/10.1038/s43246-026-01122-z.

13. H. Shi, W. Jing, W. Liu, et al., "Key Factors Governing The External Quantum Efficiency Of Thermally Activated Delayed Fluorescence Organic Light-Emitting Devices: Evidence From Machine Learning," *ACS omega* 7, no. 9 (2022): 7893–7900, https://doi.org/10.1021/acsomega.1c06820.

14. W. Zeng, H. Y. Lai, W. K. Lee, et al., "Achieving Nearly 30% External Quantum Efficiency for Orange–Red Organic Light Emitting Diodes by Employing Thermally Activated Delayed Fluorescence Emitters Composed of 1,8-Naphthalimide-Acridine Hybrids," *Advanced Materials* 30, no. 5 (2018): 1704961, https://doi.org/10.1002/adma.201704961.

15. G. Krucaite, R. Beresneviciute, D. Tavgeniene, et al., "New Bipolar Derivatives With Diphenylsulfone Or Dibenzophenone As Tadf Based Emitters For Oleds," *Organic Electronics* 125 (2024): 106981, https://doi.org/10.1016/j.orgel.2023.106981.

16. W. L. Chen, S. Y. Chen, D. C. Huang, et al., "A Method To Realize Efficient Deep-Red Phosphorescent OLEDs With a Broad Spectral Profile and Low Operating Voltages," *Materials* 14, no. 19 (2021): 5723, https://doi.org/10.3390/ma14195723.

17. P. Gnanasekaran, Y. T. Chen, Y. T. Tseng, et al., "Perceiving The Influence Of Phenyl-Carbazole Isomers On Sulfone/Thioxanthone-Based D–A–D Hosts: Realizing Efficient Red-Phosphorescent OLEDs," *Journal of Materials Chemistry C* 12, no. 6 (2024): 2203–2215, https://doi.org/10.1039/D3TC04075E.

18. V. Coropceanu, J. Cornil, D. A. da Silva Filho, Y. Olivier, R. Silbey, and J. L. Brédas, "Charge Transport In Organic Semiconductors," *Chemical reviews* 107, no. 4 (2007): 926–952, https://doi.org/10.1021/cr050140x.

19. N. Karl, "Charge Carrier Transport In Organic Semiconductors," *Synthetic Metals* 133 (2003): 649–657, https://doi.org/10.1016/S0379-6779(02)00398-3.

20. O. Dimitriev, A. Fedoryak, Y. Piryatinski, et al., "Storage Of Thermal Energy Using A Piezochromic Property of TADF Materials," *Applied Physics Letters* 128, no. 7 (2026): 073902, https://doi.org/10.1063/5.0311208.

21. H. C. Hsu, Y. P. Lin, C. H. Yeh, S. H. Wu, and C. F. Shih, "Patterned Electrode Strategy for Advanced Light Management and Enhanced Photovoltaics Efficiency in Large-Area 4T Perovskite/Silicon Tandem Solar Modules," *Solar RRL* 9, no. 18 (2025): 202500372, https://doi.org/10.1002/solr.202500372.

22. J. D. Springsteen, N. C. Giebink, and S. R. Forrest, "Nanoscale Electroluminescence Inhomogeneity and Blinking in Organic Light-Emitting Diodes," *Nature Photonics* 20 (2026): 563–570, https://doi.org/10.1038/s41566-026-01867-6.

Supporting Information

Additional supporting information can be found online in the Supporting Information section.

Supporting File: admi70655-sup-0001-SuppMat.docx.